

Testing the turbulent origin of the stellar initial mass function

Donghee G. Nam ¹★, Christoph Federrath ^{1,2} and Mark R. Krumholz ^{1,2}¹Research School of Astronomy and Astrophysics, Australian National University, Canberra, ACT 2611, Australia²ARC Centre of Excellence for Astronomy in Three Dimensions (ASTRO-3D), Canberra, ACT 2611, Australia

Accepted 2021 February 12. Received 2021 February 9; in original form 2020 September 6

ABSTRACT

Supersonic turbulence in the interstellar medium (ISM) is closely linked to the formation of stars; hence, many theories connect the stellar initial mass function (IMF) with the turbulent properties of molecular clouds. Here, we test three turbulence-based IMF models (by Padoan and Nordlund, Hennebelle and Chabrier, and Hopkins) that predict the relation between the high-mass slope (Γ) of the IMF, $dN/d \log M \propto M^\Gamma$, and the exponent n of the velocity power spectrum of turbulence, $E_v(k) \propto k^{-n}$, where $n \approx 2$ corresponds to typical ISM turbulence. Using hydrodynamic simulations, we drive turbulence with an unusual index of $n \approx 1$, measure Γ , and compare the results with $n \approx 2$. We find that reducing n from 2 to 1 primarily changes the high-mass region of the IMF (beyond the median mass), where we measure high-mass slopes within the 95 per cent confidence interval of $-1.5 < \Gamma < -1$ for $n \approx 1$ and $-3.7 < \Gamma < -2.4$ for $n \approx 2$, respectively. Thus, we find that $n = 1$ results in a significantly flatter high-mass slope of the IMF, with more massive stars formed than for $n \approx 2$. We compare these simulations with the predictions of the three IMF theories. We find that while the theory by Padoan and Nordlund matches our simulations with fair accuracy, the other theories either fail to reproduce the main qualitative outcome of the simulations or require some modifications. We conclude that turbulence plays a key role in shaping the IMF, with a shallower turbulence power spectrum producing a shallower high-mass IMF, and hence more massive stars.

Key words: hydrodynamics – turbulence – methods: numerical – stars: luminosity function, mass function – ISM: clouds.

1 INTRODUCTION

The stellar initial mass function (IMF), which describes the mass distribution of stars in a population at birth, plays a vital role in many fields of astrophysics. The literature generally agrees that the IMF has a power-law form $dN/d \log M \propto M^\Gamma$ in the high-mass end, with $\Gamma \approx -1.35$ (Salpeter 1955), while there is an ongoing debate on the possible variations in observational estimates of the slope Γ for extragalactic populations (Bastian, Covey & Meyer 2010; Krumholz 2014; Offner et al. 2014; Hopkins 2018).

One popular candidate for determining the physics of the IMF is turbulence – this is because the spectra of the molecular interstellar medium (ISM), where stars are born, provide clear evidence for supersonic turbulent motions (Larson 1981; Ossenkopf & Mac Low 2002; Elmegreen & Scalo 2004; Heyer & Brunt 2004; Roman-Duval et al. 2011). Thus, many theoretical models of the stellar IMF are based on the statistics of supersonic turbulence. Padoan, Nordlund & Jones (1997) and Padoan & Nordlund (2002, hereafter PN02) proposed that supersonic shocks create dense cores by sweeping through the ISM and compressing the gas. They then estimated the likelihood of the cores to be Jeans unstable and hence the mass distribution of collapsing cores, which may be closely linked to the IMF (André et al. 2010; Offner et al. 2014; Guszejnov & Hopkins 2015). Hennebelle & Chabrier (2008, hereafter HC08) and Hopkins (2012, hereafter H12) proposed derivations of the IMF using the Press & Schechter (1974) and excursion-set (Bond et al. 1991) formalisms,

respectively. In these models, one estimates the density variance as a function of size scale, and then determines the IMF by measuring the mass distribution of regions where the density is high enough for gravity to overcome various supporting mechanisms (such as thermal motions, turbulence, magnetic fields, and/or disc shear). The turbulence-regulated theories of the IMF by PN02, HC08, and H12 yield estimates for Γ that are generally in good agreement with observed IMFs (Miller & Scalo 1979; Kroupa 2001; Chabrier 2003, 2005; Kroupa et al. 2013; Offner et al. 2014), if the parameters are chosen carefully.

In these analytical models, the power-law index n of the turbulent velocity power spectrum,¹ $E_v(k) \propto k^{-n}$, appears as a critical factor that determines the high-mass power-law slope Γ . The narrow range of n in nature ($5/3 \leq n < 2$; Federrath 2013) can be used to argue for the relatively universal high-mass slope of the IMF produced by these models and seen in observations. However, the near universality of n also makes it difficult to test any particular model’s prediction for the relationship between n and the IMF. While the underlying functional relationship between n and the IMF shape is fundamentally different in the different models, the small range of variation in n yields a similarly small range in predicted IMFs.

None the less, a handful of simulations have explored this question. Bate (2009) studied the effect of n on the star formation within a collapsing molecular cloud by carrying out simulations with initial turbulent velocity fields characterized by $n = 2$ and $n = 4$, and

* E-mail: u6836819@anu.edu.au

¹We define $E(k)$ to be the one-dimensional power spectrum, so that Kolmogorov turbulence corresponds to $n = 5/3$.

concluded that the resultant IMFs show little dependence on n overall. Delgado-Donate, Clarke & Bate (2004) conducted a set of similar simulations but in the context of low-mass ($5 M_{\odot}$) core fragmentation, and also found that the initial choice of n does not significantly affect the stellar IMF. Goodwin, Whitworth & Ward-Thompson (2006), on the contrary, found that a shallower velocity power spectrum (n closer to zero) leads to more fragmentation in their simulations of low-mass ($\sim 5 M_{\odot}$) cores, although the statistical argument is weak due to the low number of sink particles used for the analysis ($N_{\text{sink}} < 100$). In the studies mentioned above, the authors varied only the initial velocity field, while the star formation commenced roughly after one free-fall time. The problem with this approach is that without continuous driving, most of the turbulent energy would dissipate away within a free-fall time (Mac Low et al. 1998; Stone, Ostriker & Gammie 1998; Elmegreen & Scalo 2004; McKee & Ostriker 2007), and n would relax to the natural range of 5/3 to 2. Therefore, while the choice of n could affect the initial structure of the collapsing cloud, it would have little effect during the process of star formation. We conclude that the studies are insufficient for a direct comparison with the turbulent fragmentation theories.

The aim of this work is to test how well the turbulence-regulated IMF theories (PN02, HC08, and H12) predict the high-mass power-law slope of the IMF, by simulating star formation under hydrodynamic turbulence (i.e. without magnetic fields) with velocity power spectral index n much different from what is observed in nature (5/3 to 2). We develop a turbulence driving module that is capable of driving and maintaining supersonic turbulence with arbitrary $n < 2$, and create an artificial molecular cloud with $n = 1$ in the computational domain. We measure the mass function of the stars, represented by sink particles, born under the $n = 1$ turbulence, and compare it with the IMF from the typical $n \approx 2$ supersonic turbulence. We assure the statistical significance of the study by collecting around 1000 stars represented by ‘sink particles’ per set-up through repeated simulations with different randomization of the turbulence driving.

We note that the interaction between magnetic fields and the IMFs represents another point of difference that can be used to test the models. Magnetohydrodynamic (MHD) simulations show that magnetic fields have a variety of effects, including reducing the star formation rate (SFR) and changing how gas fragments (Padoan, Haugbølle & Nordlund 2014; Federrath 2015; Haugbølle, Padoan & Nordlund 2018; Krumholz & Federrath 2019). However, they are incorporated into IMF theories in different ways. In the PN02 model, the presence of magnetic fields changes to which extent supersonic shocks compress the medium, which changes the mass spectrum of the density structures that may go on to collapse and form stars, whereas in the HC08 and H12 models the primary role of magnetic fields is to provide an additional form of pressure that makes it more difficult for structures to collapse. Although we present only hydrodynamic simulations here, in a forthcoming paper we explore the effects of magnetic fields as a complementary way of testing IMF theories.

The rest of the paper is organized as follows. We describe the simulation set-up and the initial conditions in Section 2, and present the results in Section 3. In Section 4, we compare our mass functions with the three turbulence-based IMF theories. We summarize our findings in Section 5.

2 NUMERICAL METHODS

We simulate star formation within a turbulent, dense molecular cloud with the FLASH4 adaptive mesh refinement (AMR) code

(Fryxell et al. 2000). Here, we use the HLL5R approximate Riemann solver (Bouchut, Klingenberg & Waagan 2010; Waagan, Federrath & Klingenberg 2011) and the multigrid Poisson gravity solver (Ricker 2008) on a block-based PARAMESH AMR grid. We explain the turbulence driving method in Section 2.1 and the sink particles in Section 2.2, and then we outline the initial conditions and simulation procedure in Section 2.3.

2.1 Turbulence driving

In order to drive turbulence with a prescribed velocity power spectrum of slope n , we add a time-varying acceleration field $\mathbf{F}_{\text{stir}}(\mathbf{x}, t)$ as a source term in the momentum equation (Federrath et al. 2010a). We utilize an Ornstein–Uhlenbeck process (Eswaran & Pope 1988) to construct the driving field \mathbf{F}_{stir} with an autocorrelation time matching the turbulent crossing time $T = L/2\sigma_v$, where σ_v is the rms velocity dispersion. Inspired by observations (e.g. Ossenkopf & Mac Low 2002; Elmegreen & Scalo 2004; Brunt, Heyer & Mac Low 2009), the usual procedure is to construct \mathbf{F}_{stir} with only large-scale modes (i.e. to drive at wavenumbers² $k = |\mathbf{k}| \sim 2$) and let small-scale turbulence emerge naturally. The energy cascade in (supersonic) turbulence will distribute energy to smaller scales in such a way as to produce $n \approx 2$ (Federrath 2013).

Here, however, we want to construct velocity power spectra with n significantly smaller than 2, in order to test theoretical predictions for the dependence of the IMF on n . Thus, we must inject energy on every resolvable scale, or in other words, the driving field needs to contain modes up to $k_N = L/(2\Delta x)$, where Δx is the minimum computational cell size of the simulation. However, including all wavevectors within $2 \leq k \leq k_N$ is expensive since FLASH evaluates the acceleration field at each cell from the set of driving modes, and the number of modes in a wavenumber bin $[k, k + dk]$ is proportional to $k^2 dk$. To reduce the computational load, we take a heuristic approach by generating a stirring field that contains only a fraction of randomly selected wavevectors, such that the number of modes between k and $k + dk$ scales as $k^{0.5} dk$. This practice yields a significant gain in speed (by a factor of $\sim 10^3$) while preserving the isotropy of \mathbf{F}_{stir} , and therefore the isotropy of the turbulence. The resultant driving field is constructed to have a natural mixture of solenoidal and compressive modes, which corresponds to the driving parameter $b \sim 0.4$ (Federrath et al. 2010a).

In order to run a set of simulations in which the power spectrum of the turbulent velocity field follows a power law with index $n = 1$ or $n = 2$, we construct the acceleration field \mathbf{F}_{stir} with 2.3×10^4 modes, randomly selected within $2 \leq k \leq 256$. We show below that when the amplitude of each mode $A(\mathbf{k})$ is proportional to $k^{-0.9}$, the resulting turbulence power spectrum reaches a slope close to $n = 1$. For the $n = 2$ case, we use the same method, but with $A(\mathbf{k}) \propto k^{-2}$ to match the shape of the power spectrum of \mathbf{F}_{stir} to that of the turbulent velocity typically observed in molecular clouds and simulations of supersonic turbulence (Elmegreen & Scalo 2004; McKee & Ostriker 2007; Federrath 2013). Below we refer to simulations run with a driving field $A(\mathbf{k}) \propto k^{-0.9}$ as N1 simulations, and those run with $A(\mathbf{k}) \propto k^{-2}$ as N2 simulations. We show in Appendix A that the results we obtain for the N2 simulations using this driving procedure are nearly identical to those produced via the more common procedure of driving only at low k (Federrath et al. 2010a), and allowing modes at higher k to be produced by the turbulent cascade.

²In this paper, k is measured in units of the inverse box size, so $k = 1$ corresponds to a mode with wavelength equal to the box scale L .

2.2 Sink particles and AMR

In order to follow local collapse and accretion of gas, we use the sink particle method developed in Krumholz, McKee & Klein (2004) and extended by Federrath et al. (2010b). Truelove et al. (1997) showed that the local Jeans length $\lambda_J = (\pi c_s^2 / G \rho)^{1/2}$, where c_s is the sound speed, must be resolved with at least four grid cells to prevent artificial fragmentation of the collapsing gas. The sink particle technique ensures that the Jeans length is always sufficiently resolved on the highest level of AMR, and that only bound and collapsing gas is turned into sink particles. Gas above the sink particle density threshold

$$\rho_{\text{sink}} = \frac{\pi c_s^2}{G \lambda_J^2} = \frac{\pi c_s^2}{G r_{\text{sink}}^2}, \quad (1)$$

with the sink particle radius $r_{\text{sink}} = 2.5 \Delta x_{\text{min}}$, is accreted, if the gas is bound and collapsing. Since not all overdense regions that satisfy the above density condition will collapse, we adopt an additional set of sink creation criteria from Federrath et al. (2010b) to avoid artificial sink particle formation.

For dense regions that are not yet on the highest level of AMR, we refine based on the local Jeans density, to better resolve the gravitational collapse. In our simulations, λ_J is resolved with at least 16 cells in all dimensions, in order to capture some solenoidal motions of the turbulence inside the Jeans scale (Federrath et al. 2011).

2.3 Simulation set-up

We simulate a small section of a molecular cloud within a three-dimensional periodic computational domain of length $L = 2$ pc, mean gas density $\rho_0 = 1.31 \times 10^{-20} \text{ g cm}^{-3}$, and thus the cloud mass $M_{\text{cloud}} = \rho_0 L^3 = 1550 M_{\odot}$. The base-grid resolution is $N_{\text{base}} = 512^3$ grid cells, with two additional levels of AMR, which leads to a maximum effective resolution of 2048^3 cells, i.e. a minimum cell size of $\Delta x \approx 200$ au. At this resolution, we cannot capture detailed small-scale structures and physics such as protostellar discs and radiative feedback. While radiative feedback may be crucial for setting the characteristic mass of the IMF (but see Bate 2009; Offner et al. 2009; Krumholz 2011; Krumholz et al. 2016; Federrath, Krumholz & Hopkins 2017; Haugbølle et al. 2018), at least in the theoretical models that we aim to test it has little effect on the high-mass slope of the IMF. We therefore focus solely on determining the role of the turbulence power spectrum for the high-mass tail of the IMF, and compare to predictions from IMF theories. We assume isothermal gas with constant global sound speed $c_s = 0.2 \text{ km s}^{-1}$, and drive the turbulence to an rms Mach number $\mathcal{M} = \sigma_v / c_s = 5$ for all simulations. This ensures that all simulations have identical total kinetic energy, and thus the same global virial parameter (Bertoldi & McKee 1992), $\alpha_{\text{vir}} = 5 \sigma_v^2 L / (6 G M) = 0.25$, and free-fall time $t_{\text{ff}} = \sqrt{3\pi / (2 G \rho_0)} = 0.58 \text{ Myr} = 0.594 T$. While our choice of mean density is a factor of 2–3 higher than the Larson (1981) relation,³ the choice of scaling cannot affect the shape of the IMF, which is the quantity of interest for us. We also emphasize that this commonly used approximation of α_{vir} is based on the uniform spherical approximation, and the geometry of our simulations is much different from a sphere of gas. The calculated value of α_{vir} based on its definition, $2E_{\text{kin}} / |E_{\text{grav}}|$, is more

³According to the Larson relation, a cloud with $L = 2$ pc has $n(\text{H}_2) = 1600 \text{ cm}^{-3}$, or $\rho_0 = 5.4 \times 10^{-21} \text{ g cm}^{-3}$; however, there is substantial scatter around this relation (Larson 1981; Falgarone, Puget & Pérault 1992).

than an order of magnitude higher than the approximated value of 0.25, and is dependent on turbulence parameters such as b and n (Federrath & Klessen 2012). This discrepancy is particularly strong for the simulations with $n = 1$, which, as we show below, develop significantly less large-scale density structure than the $n = 2$ case, and thus have weaker self-gravity than one might otherwise expect.

All simulations begin with uniform density distribution $\rho(\mathbf{x}) = \rho_0$ and zero velocity $\mathbf{v}(\mathbf{x}) = 0$. We let the supersonic turbulence grow by running the models without self-gravity for two turbulent crossing times $2T$ (Federrath & Klessen 2012), after which, gravity is turned on and sink particles are allowed to form in bound, collapsing regions of the cloud. We aim to collect around 1000 sink particles for each case to obtain tight statistical constraints on the slopes of the mass functions of the sink particles. For this reason, we run 14 simulations where we drive with a field $A(\mathbf{k}) \propto k^{-0.9}$ in order to produce $n \approx 1$ (N1A–N1N) and 8 simulations where we drive with $A(\mathbf{k}) \propto k^{-2}$ and thus produce $n \approx 2$ (N2A–N2H). Table 1 summarizes the key input parameters and derived quantities.

3 RESULTS

In this section, we analyse the results of the simulations summarized in Table 1. First, we examine the statistics of the velocity and density fields in Section 3.1, and verify that our turbulence driving method produces a range of power-law slopes as desired. We then study how the modified turbulence affects molecular cloud morphology in Section 3.2. We discuss the SFR and temporal evolution of the simulations in Section 3.3, and finally, we construct the sink mass function (SMF) and calculate its power-law slope Γ in Section 3.4. Although we carry out simulations in physical units, as described in Section 2.3, we note that, since they are isothermal, the simulations themselves are dimensionless and can be re-scaled to arbitrary length- and mass-scales. For this reason, in this section we will report all results in dimensionless units, i.e. we will report all masses as fractions of M_{cloud} , all lengths as fractions of L , and so forth, since these ratios are independent of the choice of dimensional scaling.

3.1 Velocity and density statistics

To confirm that the simulations reach the intended values of the velocity power spectral index n , we measure the velocity power spectra $E_v(k)$ of the simulations at $t = 2T$, i.e. when the turbulence would be fully developed and gravitational collapse begins. We interpolate the AMR grid to a 512^3 uniform grid (i.e. at the base-grid resolution) when calculating the power spectra. Fig. 1 shows the resulting power spectra, averaged over each set of runs, i.e. the line labelled N1 in the plot is the average power spectrum of runs N1A–N1N, and similarly for N2. For both sets of simulations, the power spectra show a power-law dependence on k over a broad range of length-scales until $k \sim 30$, beyond which numerical dissipation begins to take effect. We therefore estimate the slope of the power law by fitting the velocity power spectrum $E_v(k)$ over the range $5 \leq k \leq 30$. We find best-fitting values $E_v(k) \propto k^{-0.95 \pm 0.01}$ for N1 and $k^{-1.86 \pm 0.01}$ for N2, as shown in the top panel of Fig. 1. The value of n for N1 is in good agreement with our target, while the one for N2 is slightly shallower, because of the low target Mach number (see e.g. Kritsuk et al. 2007; Federrath et al. 2010a, for comparison). None the less, it is clearly steeper than the result for N1. We also present the compensated power spectra, in the bottom panel of Fig. 1, to better visualize the deviations from the power-law scaling. In both simulations, $E_v(k)$ follows the scaling law very well within the fitting range. We conclude that we successfully drive and

Table 1. Key simulation parameters and measured quantities.

ID	n	\mathcal{M}	N_{sink}	SFR _{ff}	m_{50}	m_{84}	m_{98}
(1)	(2)	(3)	(4)	(5)	(6)	(7)	(8)
N1							
A	0.93 ± 0.03	5.0	102	0.14	4.7×10^{-4}	1.7×10^{-3}	5.6×10^{-3}
B	0.91 ± 0.03	4.8	99	0.53	5.3×10^{-4}	1.5×10^{-3}	6.5×10^{-3}
C	0.92 ± 0.02	4.9	67	0.21	9.1×10^{-4}	2.4×10^{-3}	7.1×10^{-3}
D	0.96 ± 0.02	4.9	57	0.14	4.3×10^{-4}	5.0×10^{-3}	1.0×10^{-2}
E	0.95 ± 0.02	5.0	74	0.17	3.5×10^{-4}	1.8×10^{-3}	1.1×10^{-2}
F	0.97 ± 0.02	5.0	97	0.22	3.9×10^{-4}	2.0×10^{-3}	7.1×10^{-3}
G	0.97 ± 0.03	5.0	56	0.14	4.6×10^{-4}	2.6×10^{-3}	1.5×10^{-2}
H	0.92 ± 0.03	4.9	64	0.13	6.3×10^{-4}	3.7×10^{-3}	6.2×10^{-3}
I	0.98 ± 0.02	4.9	55	0.04	4.5×10^{-4}	2.5×10^{-3}	1.4×10^{-2}
J	0.98 ± 0.03	5.0	56	0.31	9.9×10^{-4}	4.1×10^{-3}	6.8×10^{-3}
K	0.98 ± 0.03	5.0	66	0.13	4.6×10^{-4}	3.1×10^{-3}	9.1×10^{-3}
L	0.86 ± 0.03	4.8	76	0.17	4.7×10^{-4}	2.1×10^{-3}	1.1×10^{-2}
M	0.92 ± 0.03	5.0	54	0.19	4.5×10^{-4}	3.1×10^{-3}	1.6×10^{-2}
N	0.95 ± 0.02	5.0	64	0.20	4.3×10^{-4}	3.8×10^{-3}	7.4×10^{-3}
Total	0.95 ± 0.01	4.9 ± 0.1	987		4.9×10^{-4}	2.5×10^{-3}	1.0×10^{-2}
N2							
A	1.80 ± 0.01	5.2	114	0.27	5.0×10^{-4}	1.9×10^{-3}	4.3×10^{-3}
B	1.87 ± 0.01	4.5	110	0.30	6.3×10^{-4}	1.8×10^{-3}	3.3×10^{-3}
C	1.89 ± 0.01	4.9	137	0.40	4.7×10^{-4}	1.3×10^{-3}	3.4×10^{-3}
D	1.89 ± 0.01	4.7	112	0.30	6.3×10^{-4}	1.6×10^{-3}	3.1×10^{-3}
E	1.91 ± 0.01	4.7	126	0.34	4.7×10^{-4}	1.4×10^{-3}	3.6×10^{-3}
F	1.84 ± 0.01	5.0	113	0.36	3.8×10^{-4}	1.6×10^{-3}	5.7×10^{-3}
G	1.87 ± 0.01	4.8	109	0.39	5.0×10^{-4}	1.9×10^{-3}	3.1×10^{-3}
H	1.85 ± 0.01	4.7	105	0.32	5.7×10^{-4}	1.7×10^{-3}	4.4×10^{-3}
Total	1.86 ± 0.01	4.8 ± 0.2	926		5.0×10^{-4}	1.7×10^{-3}	4.0×10^{-3}

Notes. (1) Simulation name; (2, 3) power-law index n and rms Mach number \mathcal{M} measured after two turbulent crossing times; (4, 5) the number of sink particles and SFR per free-fall time recorded at the SFE of 10 per cent; (6–8) 50th, 84th, and 98th percentiles of the SMF, where masses are measured as $m = M_{\text{sink}}/M_{\text{cloud}}$.

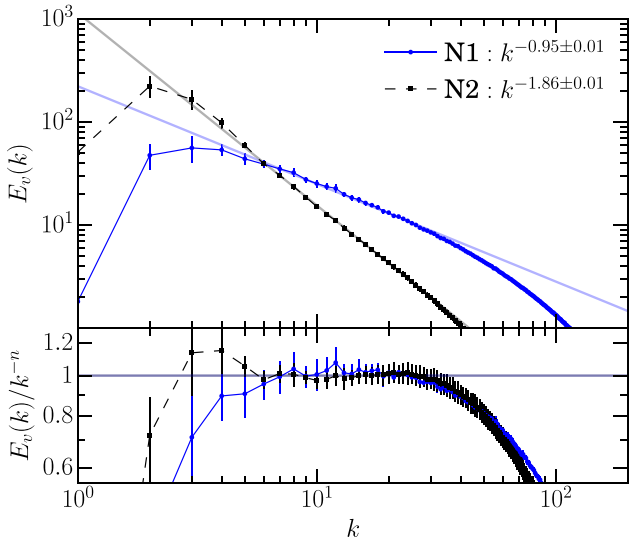


Figure 1. Turbulent velocity power spectra $E_v(k)$ (top) and the compensated power spectra $E_v(k)/k^{-n}$ (bottom), for N1 ($n = 1$; blue solid line) and N2 ($n = 1.9$; black dashed line). The vertical lines indicate the 1σ range of variation within the simulations, and the thick transparent lines in the top panel are power-law fits over the range $5 \leq k \leq 30$. The y-axes in both panels have arbitrary units, and the compensated power spectra are normalized so that their means within the fitting range are both equal to 1.

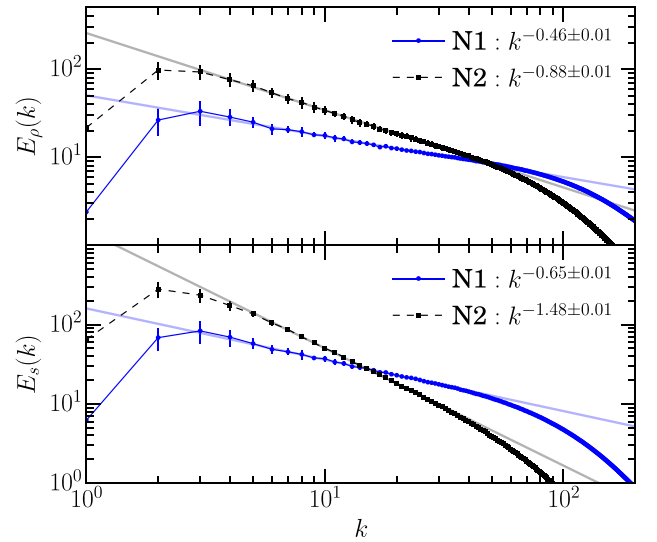


Figure 2. Power spectra of the density ρ (top) and logarithmic density $s = \ln(\rho/\rho_0)$ (bottom) for N1 and N2 runs. Symbols and fitting methods are identical to those used in Fig. 1. The y-axes have arbitrary units.

maintain turbulence such that its velocity power spectrum is a power law with an index of -1 or ≈ -2 for a broad range of length-scales, as required for the experiment we wish to perform.

In the top panel of Fig. 2, we plot the density power spectra, $E_\rho(k)$, which we measure and fit exactly as we do the

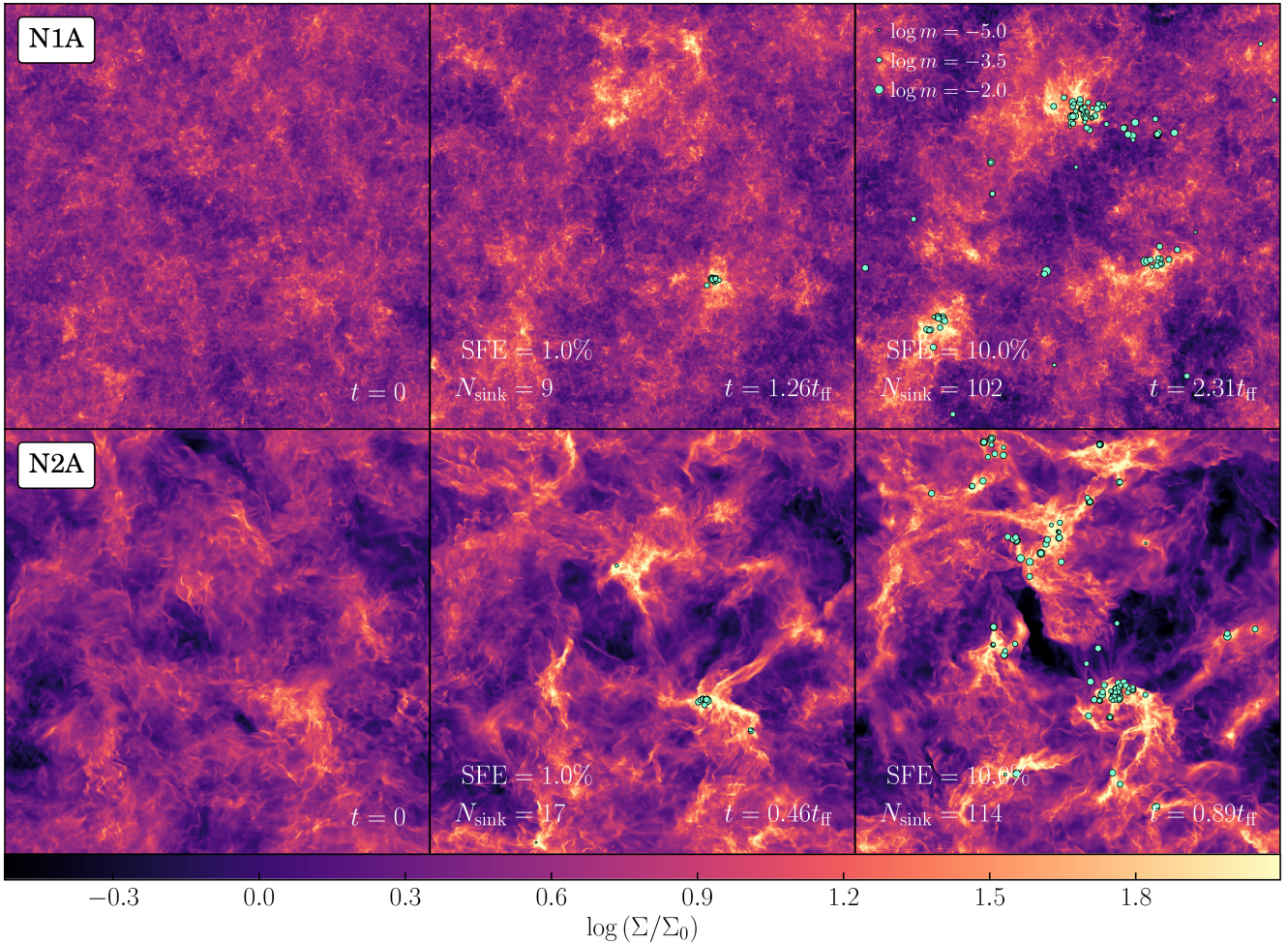


Figure 3. Column density maps extracted from N1A (top) and N2A (bottom), at the point when we turn on self-gravity (left) and at the times when the simulations reach an SFE of 1 per cent (middle) and 10 per cent (right). The colour scale is logarithmic and ranges from $\Sigma = 0.3\Sigma_0$ (black) to $125\Sigma_0$ (white), where $\Sigma_0 = \rho_0 L$. We plot sink particles as cyan circles on top of the density projections, with sizes proportional to the logarithm of their mass $m = M_{\text{sink}}/M_{\text{cloud}}$ as indicated in the legend. Panels are annotated with the number N_{sink} of sink particles present in the frame and time t of the simulation, where $t = 0$ corresponds to the time at which we turn on self-gravity.

velocity field, for N1 and N2 runs. We find turbulence with $n = 1$ has considerably less power on large spatial scales (small k) than with $n = 1.9$, due to the weaker large-scale turbulence. More interestingly, the total variance of the density fluctuations,

$$\langle \rho^2 \rangle = \int E_\rho(k) dk, \quad (2)$$

for N1 simulations is about 20 per cent lower than for the N2 counterpart, despite the fact that the total velocity fluctuation $\sigma_v^2 = (\mathcal{M}c_s)^2$ is equal in both cases.

The bottom panel of Fig. 2 shows the power spectra of the logarithmic density $s = \ln(\rho/\rho_0)$, $E_s(k)$, for N1 and N2 runs. We find the spectral index of $E_s(k)$, which we denote as $-n'$, to be $n' = 0.65 \pm 0.01$ for N1 and $n' = 1.48 \pm 0.01$ for N2. Although the exact scaling exponent of the density power spectrum remains in debate [our result for $E_\rho(k)$ is similar to that of Kim & Ryu (2005) and slightly shallower than found by Konstandin et al. (2016)], it is important to note that n' does not equal n for both simulations. This contradicts a core assumption in the HC08 model and we discuss the impact this has on the shape of the HC08 IMF in detail in Section 4.2.

3.2 Cloud structure

Fig. 3 compares the column density distributions of run N1A (top) with N2A (bottom). The left-hand panels show the structure at time $2T$, immediately before we turn on self-gravity. This figure confirms our speculations based on Fig. 2: there exist large ($k \sim 5$) density structures in the cloud with $n \approx 2$, but such structures are much less prominent in the $n = 1$ model. Instead, small-scale velocity perturbations dominate the cloud, which prevent large-scale density structures from forming. As a result the overall level of density perturbation in N1A is smaller than in N2A, which explains why the integral of $E_\rho(k)$ is lower for $n = 1$.

The dominance of small-scale turbulence in N1A continues after the self-gravity is switched on, as shown in the middle and right-hand panels of Fig. 3. While the standard supersonic turbulence ($n \approx 2$) allows gas to collapse into dense filaments, inside which dense protostellar cores emerge, gas in the $n = 1$ turbulence collapses in a fairly different manner. We no longer observe gas filaments, but dense, quasi-spherical patches of gas, and fragmentation happens inside these patches. There are two explanations for the lack of gas filaments: run N1A lacks low- k supersonic shocks that compresses gas in one dimension over large spatial scales, and the excessive

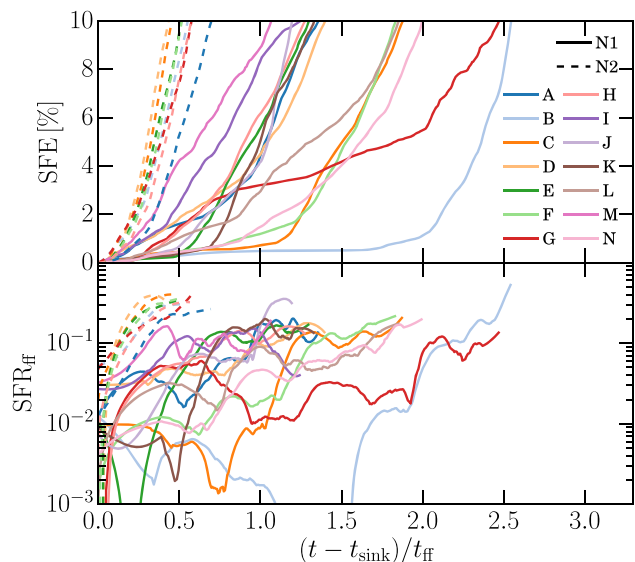


Figure 4. SFE (top) and SFR measured per free-fall time (bottom) plotted as a function of time since the formation of the first sink particle, which we denote t_{sink} . Solid lines are simulations with $n = 1.9$ and dashed lines are for $n = 1$. In general, N1 simulations evolve more slowly than N2 simulations and have lower SFRs.

amount of turbulent energy in high- k modes would quickly destroy the filaments.

3.3 Star formation rate

We note in Fig. 3 that star formation is much slower in turbulence with $n = 1$. N2A arrives at a star formation efficiency (SFE = $M_{\text{sink}}/M_{\text{cloud}}$) of 10 per cent after $0.89 t_{\text{ff}}$, whereas it takes $2.31 t_{\text{ff}}$ for N1A to convert the same amount of mass into sinks. In order to show that this is a general result and not just the case for N1A versus N2A, we plot the temporal evolution of the SFE and the SFR measured per free-fall time $\text{SFR}_{\text{ff}} = \text{dSFE}/\text{d}(t/t_{\text{ff}})$ for all our simulations in Fig. 4. We observe that it takes an average of approximately 0.5 free-fall times for the N2 simulations to go from the formation of their first sink particle to the time when the SFE reaches 10 per cent and we stop the simulation, whereas this number grows to $\sim 1.7 t_{\text{ff}}$ for N1 simulations. Similarly, we see that turbulence with $n = 1$ keeps $\text{SFR}_{\text{ff}} \lesssim 0.2$ throughout most of the simulations, while for the N2 simulations with $n = 1.9$ we have $\text{SFR}_{\text{ff}} \sim 0.3$.

One distinct and noteworthy feature is that some N1 simulations show a longer period of near-quiescence, even after the first sink particle appears, before the onset of vigorous star formation. Simulation N1B (light blue solid line in Fig. 4) is the most extreme example of this: even after the first sink forms, this run remains at $\text{SFE} \approx 0.5$ per cent for almost two free-fall times, but then the SFR_{ff} peaks at 0.54 near the end of the run. On the contrary, all N2 simulations show a much more regular pattern where star formation begins slowly, but then SFR_{ff} rapidly increases over $\lesssim 1$ free-fall time.

3.4 Mass function of the sink particles

We collect sink particles from the simulations when they reach $\text{SFE} = 10$ per cent and construct the sink mass functions (SMFs) $\text{d}N/\text{d}\log m$ for each value of n , where m is the relative mass $m =$

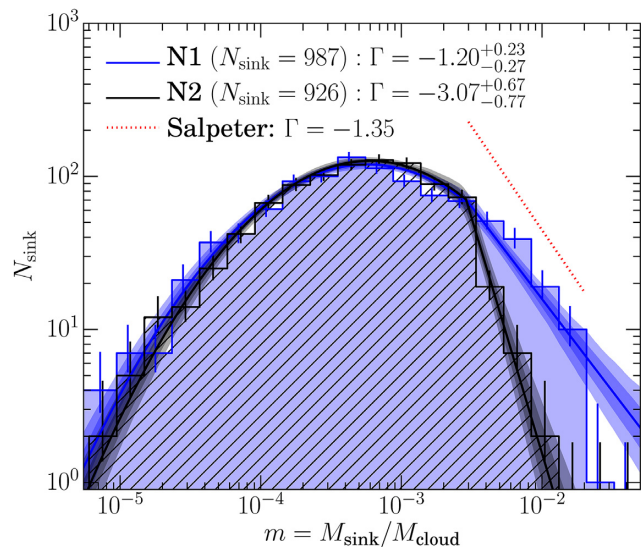


Figure 5. Logarithmic mass function $\text{d}N/\text{d}\log m$ ($m = M_{\text{sink}}/M_{\text{cloud}}$ is the sink mass relative to the cloud mass) of the sink particles from the N1 (blue shaded histogram) and N2 (black hatched histogram) simulations, at $\text{SFE} = 10$ per cent. The error bars on the histograms indicate the 68 per cent confidence interval for each bin. The solid lines show the median values of the posterior PDF obtained from the MCMC fitting, with the surrounding shaded regions representing the 68 per cent (thick shades) and 95 per cent (light shades) confidence intervals determined from the MCMC fit. We also report the median values for the high-mass power-law slope Γ , with the 2nd to 98th percentile ranges in the legend. The red dotted line corresponds to the Salpeter (1955) slope ($\Gamma = -1.35$). We find that the power-law slope of the SMFs generated from the simulations are shallower (for N1) and significantly steeper (for N2) than the Salpeter slope. Thus, the turbulence power spectrum plays a key role in controlling the high-mass slope of the IMF.

$M_{\text{sink}}/M_{\text{cloud}}$ of the sinks. Fig. 5 shows the resultant SMFs, which span three orders of magnitude in mass and thus provide a sufficient dynamic range to identify differences between the N1 and N2 cases at high confidence. Quantitatively, we form sinks as small as $m = 5 \times 10^{-7}$ ($M_{\text{sink}} = 8 \times 10^{-4} M_{\odot}$), and as large as $m = 2.5 \times 10^{-2}$ ($M_{\text{sink}} = 40 M_{\odot}$); the lower cut-off is imposed by the resolution of the simulation, while the upper one is due to the finite amount of mass contained in the periodic box. We observe that the N1 simulations generate significantly more sinks with $m \gtrsim 5 \times 10^{-3}$ than the N2 simulations. This makes the high-mass fall-off in N1 slightly shallower than that of the Salpeter (1955) IMF, while the N2 SMF shows high-mass scaling visibly steeper than the Salpeter slope. The characteristic mass where the IMF peaks ($m \approx 10^{-3}$), on the other hand, appears to be fairly insensitive to the velocity power spectral index.

We compare the cumulative mass functions for the N1 and N2 runs in Fig. 6. The figure clearly shows that the mass distributions are statistically indistinguishable below the median mass, but that the cumulative SMF for N1 is skewed significantly towards higher mass compared to that for N2. To demonstrate this quantitatively, we report the values of the 50th, 84th, and 98th percentile of the SMF in Table 1. While we find that the median masses are almost identical for N1 and N2 ($m_{50} = 4.9 \times 10^{-4}$ for N1 and 5.0×10^{-4} for N2), the 86th and 98th percentile masses widely differ, as one can find from Table 1. We also conduct a Kolmogorov–Smirnov (KS) test comparing the SMFs. If we compare only the parts of the distribution below the median mass, the test returns a p -value ($p = 0.59$), consistent with the hypothesis that the N1 and N2 data are drawn from the same parent distribution. However, if we instead

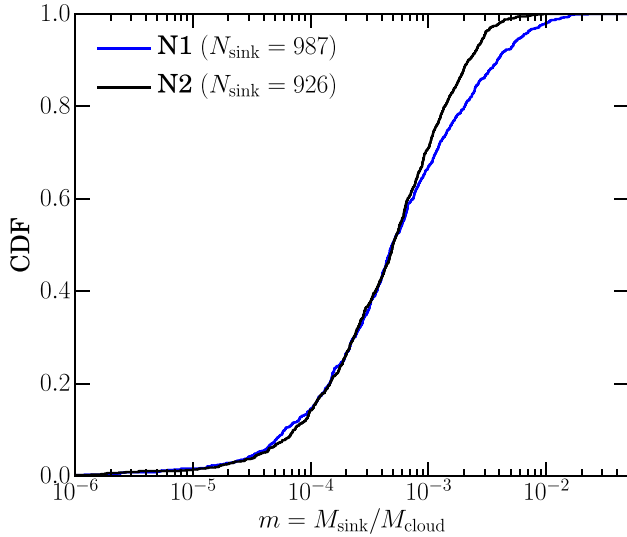


Figure 6. Cumulative distribution function (CDF) of the sink masses for N1 (blue) and N2 (black) simulations. We observe that the CDFs with $n = 1$ and 1.9 disagree only within the high-mass (beyond the median mass) region. N1 simulations produce a significantly more top-heavy CDF.

compare the full SMFs, we obtain $p \sim 10^{-8}$. These statistics provide additional evidence for our speculation that altering the turbulence spectral index primarily affects the high-mass tail of the IMF.

Finally, in order to quantitatively measure the difference in the slope of the SMFs (Γ), we use the Markov chain Monte Carlo (MCMC) sampler EMCEE (Foreman-Mackey et al. 2013) to fit the SMFs to a Chabrier (2005)-like functional form for the IMF,

$$\frac{dN}{d \log m} = A_1 \begin{cases} \frac{1}{\sqrt{2\pi\sigma^2}} \exp\left[-\frac{(\log m - \log m_0)^2}{2\sigma^2}\right], & m < m_T, \\ A_2 m^\Gamma, & m \geq m_T, \end{cases} \quad (3)$$

with four free parameters $\theta = (m_0, \sigma, m_T, \Gamma)$, where m_0 and σ are respectively the peak and standard deviation of the lognormal part, m_T is the transition point between the lognormal and power-law part, and Γ is the power-law slope. A_1 is a normalization constant, set by the total mass in stars, and A_2 is set so as to ensure continuity at m_T .⁴ The posterior probability distribution for θ is given by Bayes' Theorem,

$$P(\theta | \{m_{\text{sink}}\}) = \frac{P(\theta)P(\{m_{\text{sink}}\}|\theta)}{\int P(\theta')P(\{m_{\text{sink}}\}|\theta') d\theta'}, \quad (4)$$

where the likelihood function for a given set of parameters θ and sink masses $\{m_{\text{sink}}\}$ is

$$P(\{m_{\text{sink}}\}|\theta) = \prod_{m_i \in \{m_{\text{sink}}\}} \frac{dN}{dm}(m_i; \theta). \quad (5)$$

In other words, $P(\{m_{\text{sink}}\}|\theta)$ is the probability density for the particular set of sink particle masses $\{m_{\text{sink}}\}$ produced in our simulations, given a proposed set of parameters θ describing the IMF. The advantage of this approach, compared to fitting a model to the histograms, is that fitting to histograms often produces results that

⁴We note that the derivative of equation (3) is not necessarily continuous at $m = m_T$. We allow this possibility to ensure that the slope we find for the power-law portion of the IMF at high masses is not forced to some particular value by a requirement that it match the slope favoured by the sub-peak sink population, which dominates the total number of sink particles, and thus the likelihood function.

are sensitive to the choice of bins, particularly in sparsely populated ranges of mass; our Bayesian approach removes the need for binning.

Fitting requires some care with respect to the choice of priors. We adopt flat, uninformative priors for m_0 , σ , and $\tan^{-1} \Gamma$, with the latter being equivalent to assuming that all angles of the power-law slope (straight line in log-log space) are equally likely (Jeffreys 1946). These choices have little impact on the results of the fit parameters. For the N2 SMF, we also adopt a flat prior for m_T , and we obtain a good fit by doing so; we show the results of our MCMC fit in comparison to the data in Fig. 5, indicating that the fit describes the data well. We find the high-mass slope $\Gamma(n = 1.9) = -3.07^{+0.67}_{-0.77}$ for N2, where the central estimate is the median of the posterior probability distribution function (PDF), and the error bars indicate the 2nd to 98th percentile confidence interval. If we adopt a similar flat, unconstrained prior for m_T for N1, we find a higher value for m_T than for N2. In order to enable a meaningful comparison of the slopes between N1 and N2, we therefore adopt an informative prior on m_T when fitting the N1 SMF, by setting it equal to a Gaussian approximation of the posterior distribution of m_T in N2.⁵ Intuitively, this amounts to saying that, in order to perform a meaningful comparison of slopes between N1 and N2, we demand that the turnover point m_T between the lognormal and power-law portions of the SMF be at similar masses. With this prior, we find $\Gamma(n = 1) = -1.20^{+0.23}_{-0.27}$ for N1. We show this fit in Fig. 5, and find that the resulting functional form is a good fit to the simulated mass distribution.

In summary, we find that the turbulence power spectrum is a key ingredient for controlling the high-mass region of the IMF, with N1 producing more massive stars than N2. The high-mass slope (Γ) of the IMF is significantly shallower for N1 compared with N2, with the Salpeter slope in between N1 and N2. We discuss possible reasons for this when we now compare the simulation results with the predictions of the IMF theories.

4 COMPARISON WITH THEORETICAL MODELS OF THE IMF

In this section, we compare the simulation results with the three turbulence-regulated IMF models: PN02 (Padoan & Nordlund 2002), HC08 (Hennebelle & Chabrier 2008), and H12 (Hopkins 2012). We summarize the comparison in Fig. 7, as well as in Table 2, which lists the high-mass IMF slopes estimated from the three theoretical models and calculated from our simulations for velocity power spectral indices of $n = 1$ and 1.9. We emphasize that we only compare the high-mass region of the IMF, and other features of the IMF such as the IMF peak and the sub-stellar mass function are out of the scope of this study, since we do not include the relevant physics in our simulations (Section 3.4).

4.1 PN02 model

In the PN02 theory, cores emerge from turbulent shocks sweeping through the molecular cloud medium, and hence the resultant IMF is dependent on the extent to which shocks compress the gas. PN02 predict that the resulting IMF will be a power law with slope

$$\Gamma = -3/(4 - n), \quad (6)$$

assuming a linear shock jump condition, i.e. shocks increase the density of the gas linearly with the Mach number of the shock

⁵To be precise, the prior distribution we adopt for m_T is $p_{\text{prior}} \propto \exp[-(m_T - m_{T,N2,\text{med}})^2 / 2\sigma_{N2}^2]$, where $m_{T,N2,\text{med}}$ is the median posterior value of m_T for our fit to N2 and σ_{N2} is half the 16th–84th percentile range for the posterior.

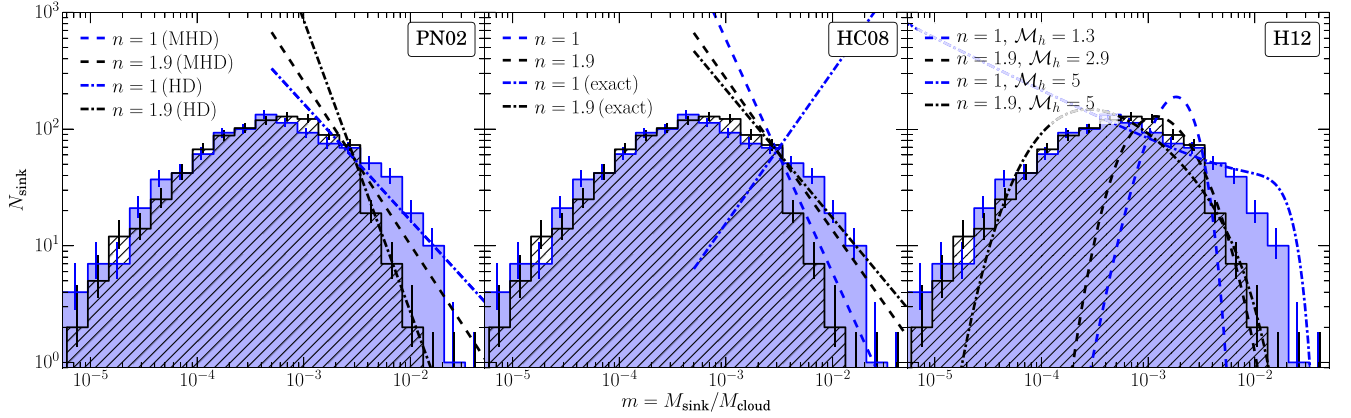


Figure 7. Comparison between the mass distributions obtained in the simulations (Fig. 5) and the high-mass IMF slopes estimated by the three IMF theories by **PN02** (left), **HC08** (middle), and **H12** (right). The blue histograms and lines correspond to the N1 ($n = 1$) simulations and the black ones correspond to the N2 ($n = 1.9$) simulations. Left-hand panel: the **PN02** model, using the MHD (dashed lines) or HD (dash-dotted lines) shock jump conditions. Note that the IMF slope is identical for $n = 1$, regardless of the choice of the jump condition. Middle panel: the IMF slopes originally presented in the **HC08** paper (dashed lines) and the slopes including the correction term as given in Hennebelle & Chabrier (2009, dash-dotted lines). For the **PN02** and **HC08** models, we anchor the power-law functions at $m = m_T = 3 \times 10^{-3}$, as obtained from the MCMC fitting of the simulation data. Right-hand panel: the IMFs predicted by the **H12** model, with the characteristic Mach number (\mathcal{M}_h) calculated from the velocity dispersion on the largest scales in our simulations, $1 < k < 3$, where $k = 1$ corresponds to the box scale L (dashed lines), or set to the rms Mach number of the simulations (dash-dotted lines). We arbitrarily shift both dashed lines to lower masses by a factor of 2 and both dash-dotted lines to lower masses by a factor of 10, compared with the direct prediction of the **H12** model, as an attempt to match the high-mass end of the SMFs with that of the corresponding IMFs.

Table 2. Predictions of the slope Γ of the high-mass tail of the IMF from turbulence-regulated IMF theories.

Model	Velocity spectral index	
	$n = 1$	$n = 1.9$
	$\Gamma =$	
PN02	-1.0	-1.4
PN02 (HD)	-1.0	-2.5
HC08	-2.0	-1.3
HC08 (exact)	+1.3	-1.1
H12 ($k = 1-3$)	-16	-2.1
H12 (rms)	-0.3	-2.0
This study	$-1.20^{+0.23}_{-0.27}$	$-3.07^{+0.67}_{-0.77}$

Notes. **PN02**: Padoan & Nordlund (2002). **PN02 (HD)**: **PN02** with hydrodynamic shock jump conditions ($\rho'/\rho = \mathcal{M}^2$). **HC08**: Hennebelle & Chabrier (2008). **HC08 (exact)**: **HC08** with the correction term discussed in Hennebelle & Chabrier (2009). **H12 ($k = 1-3$)**: Hopkins (2012), with \mathcal{M}_h derived by integrating the power spectrum from $k = 1$ to 3, and slope derived by averaging between $m = 3 \times 10^{-3}$ and 10^{-2} . **H12 (rms)**: same as **H12 ($k = 1-3$)**, but using the full rms Mach number for \mathcal{M}_h .

(hereafter ‘MHD condition’). On the other hand, Padoan et al. (2007) suggested that if there are no magnetic fields present, it is more appropriate to consider the post-shock gas density to be proportional to \mathcal{M}^2 (‘HD condition’), which leads to

$$\Gamma = -3/(5 - 2n). \quad (7)$$

In either the HD or MHD cases, **PN02** predict that a shallower velocity power spectrum produces a shallower high-mass IMF: $\Gamma(n = 1) = -1$ (for both the MHD and HD condition) and $\Gamma(n = 1.9) = -1.4$ (MHD condition) or -2.5 (HD condition). We show these theoretical predictions for Γ together with the simulation SMFs in the left-hand panel of Fig. 7. Overall, the **PN02** prediction with the HD shock jump condition (i.e. in the absence of magnetic fields) is quantitatively consistent with both N1 and N2 simulations within the 95 per cent interval range.

The n -dependence on the high-mass slope of the **PN02** model comes from the linewidth–size relation. Shocks larger in size (i.e. also with higher Mach number) can sweep up more gas and thereby produce more massive cores. However, this effect is countered by the fact that shocks with higher \mathcal{M} produce thinner compressed post-shock layers, which reduces the mass of the resultant dense core, because the core size is set equal to the post-shock length-scale in the **PN02** model. Because the velocity power spectrum controls how the velocity dispersion scales with size, namely $\mathcal{M}(\ell) \propto \ell^{(n-1)/2}$, altering n changes the mass of cores produced by a shock with fixed length, and hence changes the IMF shape. In addition, since more massive stars take longer to form because they require a larger core with a longer dynamical time, a shallower IMF is predicted for $n = 1$ in the **PN02** model, which is also consistent with our finding of a lower SFR for $n = 1$.

4.2 **HC08** model

In the **HC08** model, turbulence has two roles during the star formation process: it creates dense patches of gas that may become self-gravitating, but also provides additional turbulent energy that counteracts collapse. According to the model, decreasing n (i.e. making the power spectrum flatter) and hence enhancing turbulence on smaller scales both narrows the density PDF (i.e. creating dense regions less frequently) and increases the critical density for collapse. This prediction suggests that the SFR would be much lower for $n = 1$, consistent with our results (see Sections 3.1 and 3.3). **HC08** also predict⁶

$$\Gamma \approx -(n + 3)/(2n), \quad (8)$$

⁶Here, we note that our n is the index of the one-dimensional power spectrum, whereas **HC08** work in terms of the three-dimensional spectrum, which has index $n - 2$. Care should therefore be taken in comparing the expressions we give here to those given in **HC08**, since our n does not refer to the same quantity as the n that appears in their equations.

that is, turbulence with a shallower velocity power spectrum produces a steeper IMF, which is opposite to what is observed in our simulations (middle panel of Fig. 7).

However, Hennebelle & Chabrier (2009) suggested a correction term for equation (8):

$$\Gamma = -\frac{n+3}{2n} + \frac{3(3-n)}{n} \frac{\ln \mathcal{M}_*}{\sigma_s^2}, \quad (9)$$

where \mathcal{M}_* is the (one-dimensional) Mach number on the Jeans scale (λ_J) and σ_s^2 is the global variance in the logarithmic density s . Under usual circumstances, where $n \approx 2$ and $\mathcal{M}_* \lesssim 10$, the second term is close to zero and has only minimal effect on the overall shape of the IMF. However, for $n = 1$, the correction term becomes much more significant. We calculate the exact value of the high-mass slope predicted by HC08 with the correction term to be $\Gamma = +1.3$ for $n = 1$, given in our $n = 1$ simulations $\sigma_s^2 = 1.94$ at the beginning of gravitational collapse ($t = 2T$) and $\mathcal{M}_* = 4.9/3^{1/2} = 2.8$ (converting the 3D Mach number of ~ 4.9 in the simulations, to the 1D Mach number used in the HC model). While the correction is in the right direction, it is far larger than the difference between the measured value from our simulations and the HC08 prediction, and appears implausible, since for $\Gamma = 1.3$ the total mass in the high-mass tail of the IMF would diverge.

4.3 H12 model

The role of the velocity power spectrum in the H12 theory is similar to that in the HC08 theory. The primary difference between the theories lies in how one estimates the density PDF and counts the number of bound regions as a function of length-scale. The difference is none the less significant; for example, H12 speculates that the density variance is greater on small length-scales and smaller on large length-scales for $n \approx 1$, qualitatively similar to our results (Fig. 2), while in HC08 the density variance is smaller across all scales. Since the H12 IMF model generally does not have a closed form, one needs to follow the excursion-set formalism and directly rebuild the mass functions in order to study the effect of n in the H12 model. We therefore developed our own PYTHON code that reproduces the last-crossing IMF, and compared the results with our simulation.⁷

In the H12 theory, the power spectral index n and the characteristic Mach number \mathcal{M}_h are the two important parameters that determine the shape of the IMF. The parameter n is straightforward to define and measure in our simulations, but there is some ambiguity in how to define \mathcal{M}_h for our simulation. In the context of the H12 model, \mathcal{M}_h is the Mach number of the velocity field measured on sizes comparable to the galactic scale height, h , which is identified with the outer scale of the turbulent cascade. Our simulation does not possess a scale height, since it takes place in a periodic box, and there is some ambiguity in how to define the outer scale of the turbulence, particularly for the $n = 1$ case where turbulent power is not sharply peaked on large scales. We therefore consider two possibilities, which roughly bracket the range of reasonable choices. The first is simply to set $\mathcal{M}_h = \mathcal{M} = 5$, i.e. to set the Mach number at the outer scale of the turbulence equal to the Mach number of the simulation box as a whole. This choice is most consistent with

⁷We make one modification in our code relative to the original H12 model. In the H12 model, the barrier function includes a term representing rotational support, parametrized by the epicyclic frequency κ . Since our simulation has no systematic rotation, we take the limit $\kappa \rightarrow 0$ when evaluating the barrier function.

the implicit assumption in the H12 model that the turbulent power is mostly on large scales, so as one considers larger and larger size scale, the Mach number monotonically increases, approaching the total Mach number as the size scale under consideration approaches h . Our second method for estimating \mathcal{M}_h is to integrate the velocity power spectra in the region $1 < k < 3$, which is roughly the outer scale of the turbulence in our periodic box. Doing so, we find $\mathcal{M}_h = 1.3$ for the N1 simulations and 2.9 for the N2 simulations.

We compare the predictions of the H12 model with the aforementioned parameters to our simulations in the right-hand panel of Fig. 7 (dashed and dot-dashed lines). We first focus on the case where we measure \mathcal{M}_h by integrating over $k = 1-3$, and observe that, while the IMF predicted for $n = 1.9$ coincides fairly well with the N2 simulations for $m \gtrsim 10^{-3}$, the $n = 1$ prediction is significantly steeper than that for $n = 1.9$, which is the opposite of what we observe from our simulations. By contrast, if we accept a mass shifting factor⁸ of 10, the predicted IMF shapes beyond the peaks are significantly closer to what we measure for both the N1 and N2 simulations in the case where we take $\mathcal{M}_h = \mathcal{M} = 5$ (dash-dotted lines), except near $m \approx 10^{-2}$. The predicted qualitative effect of varying n is also consistent with our simulation results, and with Hopkins (2013). According to the H12 model, the cut-off in the N1 SMF beyond $m > 10^{-2}$, which is most likely a result of the finite mass in the simulation box, is explained by the suppression of density fluctuations due to mass conservation. However, we caution that, because of the ambiguity in the definition of \mathcal{M}_h inherent in the H12 models, as well as the necessity of an arbitrary horizontal shift, we can only tentatively identify this as a successful prediction. Finally, we note that while the H12 model in principle allows for the inclusion of magnetic fields, the dependence of the IMF on the magnetic field has not been studied in detail in Hopkins (2013). We aim to quantify the effects of the magnetic field on the IMF in a follow-up study.

5 CONCLUSIONS

Using hydrodynamical simulations that include gravity and sink particles, we investigate the effect of the shape of the power spectrum of supersonic turbulence [$E_v(k) \propto k^{-n}$] on the stellar IMF. With the help of AMR and repeated simulations with different random seeds for the turbulence, we construct statistically significant sink mass distributions with 900–1000 sink particles formed for each n , and a dynamic range spanning three orders of magnitude, from a low-mass cut-off imposed by the grid resolution to a high-mass cut-off imposed by the finite size of the simulation domain. From the sink particle populations, we find that turbulence with $n = 1$ significantly flattens the high-mass end of the IMF compared to $n \approx 2$ (i.e. $n = 1$ turbulence generates more massive stars), but has little effect on the distribution of low-mass stars and sub-stellar objects. This result is consistent with our current understanding of molecular cloud dynamics and star formation: turbulence governs the large-scale fragmentation of molecular clouds, while other mechanisms such as radiative heating play more important roles below a certain length-scale (or mass-scale). We also find that compared to natural supersonic turbulence with $n \approx 2$, turbulence with a scaling index of $n = 1$ creates less density dispersion, does not promote the formation of large-scale gas structures such as large-scale filaments, and slows down the SFR.

⁸A possible justification for this shift is that in our simulations there are no density fluctuations at the box scale, whereas in the H12 model fluctuations at the galactic scale height h are non-zero, and only damp to zero on scales $\ll h$ (e.g. Hopkins 2013, fig. 2).

We compare our simulation results with three turbulence-regulated theoretical models of the IMF: **PN02**, **HC08**, and **H12**. We find that the qualitative predictions of the three models vary significantly (e.g. the dependence of the high-mass slope of the IMF on n). Out of the three IMF models, we find that the **PN02** theory is consistent with our measurement of the n -dependence of the high-mass IMF slope (Γ). The density statistics predicted by the **HC08** model agree qualitatively with our observations, but their predicted high-mass slope diverges for $n \rightarrow 1$. We find that the **H12** model can be made similar to our simulated IMFs in the high-mass range. However, the model is quite sensitive to the choice of the definition of a key parameter (\mathcal{M}_h), which is defined somewhat ambiguously in the model, and if we adopt an alternative definition, the **H12** theory predicts qualitatively different results that disagree with our simulations.

There remains one important question that is not yet answered: why did turbulence with $n \approx 2$ shape a high-mass IMF much steeper than the Salpeter IMF in our simulations? As mentioned in Sections 1 and 4.1, the answer may be the absence of magnetic fields, since only the **PN02** theory successfully predicts the high-mass slope for the $n \approx 2$ hydrodynamical turbulence (apart from the modified **H12** theory with $\mathcal{M}_h = 5$), and it is the only model that explicitly encodes the role of magnetic fields in shaping the high-mass IMF. We suggest a follow-up study that includes varying levels of magnetic fields, in order to quantify the role of the magnetic field in the shape of the IMF.

ACKNOWLEDGEMENTS

We thank Åke Nordlund for providing a detailed and constructive referee report. We also thank Patrick Hennebelle and Paolo Padoan for their interest, comments, and suggestions on the manuscript. We further thank Phil Hopkins and Dávid Guszejnov for their help with reproducing the **H12** IMF model. CF acknowledges funding provided by the Australian Research Council (Discovery Project DP170100603 and Future Fellowship FT180100495) and the Australia–Germany Joint Research Cooperation Scheme (UA-DAAD). MRK acknowledges funding from the Australian Research Council (Discovery Project DP190101258 and Future Fellowship FT180100375) and the Australia–Germany Joint Research Cooperation Scheme (UA-DAAD). We further acknowledge high-performance computing resources provided by the Leibniz Rechenzentrum and the Gauss Centre for Supercomputing (GCS; grants pr32lo, pr48pi, and GCS large-scale project 10391), and the Australian National Computational Infrastructure (grants ek9 and jh2) in the framework of the National Computational Merit Allocation Scheme and the Australian National University Merit Allocation Scheme. The simulation software FLASH was in part developed by the Department of Energy-supported Flash Center for Computational Science at the University of Chicago.

DATA AVAILABILITY

The simulation data underlying this article will be shared on reasonable request to Donghee Nam at u6836819@anu.edu.au. Our PYTHON code that reproduces the **H12** last-crossing IMF is publicly available at <https://github.com/dongheenam/hopkins-imf>.

REFERENCES

André P. et al., 2010, *A&A*, 518, L102
Bastian N., Covey K. R., Meyer M. R., 2010, *ARA&A*, 48, 339

- Bate M. R., 2009, *MNRAS*, 397, 232
Bertoldi F., McKee C. F., 1992, *J. Chem. Inf. Model.*, 395, 140
Bond J. R., Cole S., Efstathiou G., Kaiser N., 1991, *ApJ*, 379, 440
Bouchut F., Klingenberg C., Waagan K., 2010, *Numer. Math.*, 115, 647
Brunt C. M., Heyer M. H., Mac Low M.-M., 2009, *A&A*, 504, 883
Chabrier G., 2003, *PASP*, 115, 763
Chabrier G., 2005, in Corbelli E., Palle F., eds, *Astrophysics and Space Science Library*, Vol. 327, *The Initial Mass Function 50 Years Later*. Springer-Verlag, Berlin, p. 41
Delgado-Donate E. J., Clarke C. J., Bate M. R., 2004, *MNRAS*, 347, 759
Elmegreen B. G., Scalo J., 2004, *ARA&A*, 42, 211
Eswaran V., Pope S. B., 1988, *Comput. Fluids*, 16, 257
Falgarone E., Puget J.-L., Pérault M., 1992, *A&A*, 257, 715
Federrath C., 2013, *MNRAS*, 436, 1245
Federrath C., 2015, *MNRAS*, 450, 4035
Federrath C., Klessen R. S., 2012, *ApJ*, 761, 156
Federrath C., Roman-Duval J., Klessen R., Schmidt W., Mac Low M. M., 2010a, *A&A*, 512, A81
Federrath C., Banerjee R., Clark P. C., Klessen R. S., 2010b, *ApJ*, 713, 269
Federrath C., Sur S., Schleicher D. R., Banerjee R., Klessen R. S., 2011, *ApJ*, 731, 62
Federrath C., Krumholz M., Hopkins P. F., 2017, *J. Phys. Conf. Ser.*, 837, 012007
Federrath C., Klessen R. S., Iapichino L., Beattie J. R., 2020, preprint ([arXiv:2011.06238v1](https://arxiv.org/abs/2011.06238v1))
Foreman-Mackey D., Hogg D. W., Lang D., Goodman J., 2013, *PASP*, 125, 306
Fryxell B. et al., 2000, *ApJS*, 131, 273
Goodwin S. P., Whitworth A. P., Ward-Thompson P., 2006, *A&A*, 452, 487
Guszejnov D., Hopkins P. F., 2015, *MNRAS*, 450, 4137
Haugbølle T., Padoan P., Nordlund Å., 2018, *ApJ*, 854, 35
Hennebelle P., Chabrier G., 2008, *ApJ*, 684, 395 (HC08)
Hennebelle P., Chabrier G., 2009, *ApJ*, 702, 1428
Heyer M. H., Brunt C. M., 2004, *ApJ*, 615, L45
Hopkins P. F., 2012, *MNRAS*, 423, 2037 (H12)
Hopkins P. F., 2013, *MNRAS*, 430, 1653
Hopkins A. M., 2018, *Publ. Astron. Soc. Aust.*, 35, e039
Jeffreys H., 1946, *Proc. R. Soc. A*, 186, 453
Kim J., Ryu D., 2005, *ApJ*, 630, L45
Konstantin L., Schmidt W., Girichidis P., Peters T., Shetty R., Klessen R. S., 2016, *MNRAS*, 460, 4483
Kritsuk A. G., Norman M. L., Padoan P., Wagner R., 2007, *ApJ*, 665, 416
Kroupa P., 2001, *MNRAS*, 322, 231
Kroupa P., Weidner C., Pflamm-Altenburg J., Thies I., Dabringhausen J., Marks M., Maschberger T., 2013, in Oswald T. D., Gilmore G., eds, *Planets, Stars Stellar Syst. Vol. 5*. Springer Science + Business Media, Springer, Dordrecht, p. 115
Krumholz M. R., 2011, *ApJ*, 743, 110
Krumholz M. R., 2014, *Phys. Rep.*, 539, 49
Krumholz M. R., Federrath C., 2019, *Front. Astron. Space Sci.*, 6, 7
Krumholz M. R., McKee C. F., Klein R. I., 2004, *ApJ*, 611, 399
Krumholz M. R., Myers A. T., Klein R. I., McKee C. F., 2016, *MNRAS*, 460, 3272
Larson R. B., 1981, *MNRAS*, 194, 809
McKee C. F., Ostriker E. C., 2007, *ARA&A*, 45, 565
Mac Low M., Smith M. D., Klessen R. S., Burkert A., 1998, *Ap&SS*, 261, 195
Mathew S. S., Federrath C., 2020, *MNRAS*, 496, 5201
Miller G. E., Scalo J. M., 1979, *ApJS*, 41, 513
Offner S. S., Klein R. I., McKee C. F., Krumholz M. R., 2009, *ApJ*, 703, 131
Offner S. S. R., Clark P. C., Hennebelle P., Bastian N., Bate M. R., Hopkins P. F., Moraux E., Whitworth A. P., 2014, *Protostars Planets VI*. University of Arizona Press, Tucson, p. 53
Ossenkopf V., Mac Low M.-M., 2002, *A&A*, 390, 307
Padoan P., Nordlund Å., 2002, *ApJ*, 576, 870 (PN02)
Padoan P., Nordlund Å., Jones B. J. T., 1997, *MNRAS*, 288, 145
Padoan P., Nordlund Å., Kritsuk A. G., Norman M. L., Li P. S., 2007, *ApJ*, 661, 972

- Padoan P., Haugbølle T., Nordlund Å., 2014, *ApJ*, 797, 32
 Press W. H., Schechter P., 1974, *ApJ*, 187, 425
 Ricker P. M., 2008, *ApJS*, 176, 293
 Roman-Duval J., Federrath C., Brunt C., Heyer M., Jackson J., Klessen R. S., 2011, *ApJ*, 740, 120
 Salpeter E. E., 1955, *ApJ*, 121, 161
 Stone J. M., Ostriker E. C., Gammie C. F., 1998, *ApJ*, 508, L99
 Truelove J. K., Klein R. I., McKee C. F., Holliman J. H., II, Howell L. H., Greenough J. A., 1997, *ApJ*, 489, L179
 Waagan K., Federrath C., Klingenberg C., 2011, *J. Comput. Phys.*, 230, 3331

APPENDIX A: EFFECT OF TURBULENT DRIVING RANGE ON THE IMF SHAPE

Here, we compare the N2 simulations, in which the turbulence is driven with $n \approx 2$ over an extended wavenumber range of $2 \leq k \leq 256$, with an additional set of simulations in which only large-scale modes ($1 < k < 3$) are excited and the turbulent cascade naturally populates the small-scale modes (i.e. as in Federrath 2015; Mathew & Federrath 2020, for example). We run four simulations with this large-scale driving (hereafter denoted as *para* simulations) to check the effect of our turbulence driving method on the velocity power spectra and the IMF.

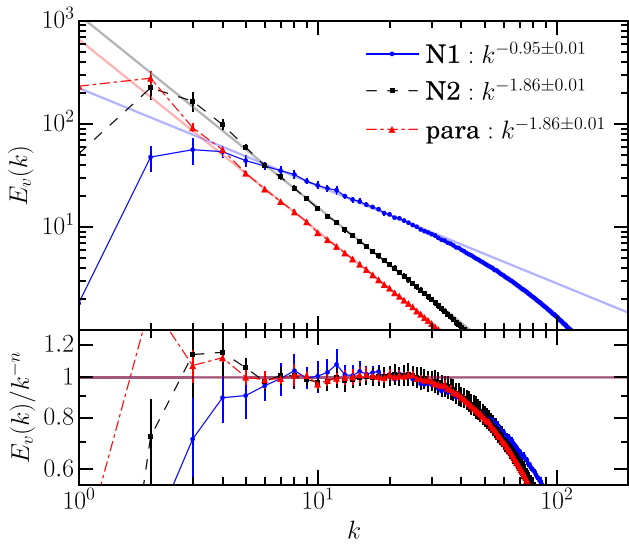


Figure A1. Turbulent velocity power spectra $E_v(k)$ (top) and the compensated power spectra $E_v(k)/k^{-n}$ of the N1 (blue solid line), N2 (black dashed line), and *para* (red dash-dotted line) simulations. The errorbars and fitting methods are identical to those used in Fig. 1.

In Fig. A1, we show the velocity power spectra of the N1, N2, and *para* simulations. We measure the scaling exponent of the velocity power spectrum in the *para* simulations and find $E_v(k) \propto k^{-1.86 \pm 0.01}$, which is identical to that in the N2 simulations. The *para* simulations have more power in very large modes ($k = 1-2$) compared to the N2 simulations because most of the energy is injected on those scales. In Fig. A2, we compare the SMFs from the three simulation sets. We find that the SMFs from the N2 and *para* simulations are statistically indistinguishable. Therefore, we conclude that the choice of the turbulent driving range for $n \approx 2$ does not affect the mass distribution of sink particles formed in simulations with $n \approx 2$, as this is the turbulence exponent that naturally arises when driving supersonic turbulence on large scales (Federrath 2013; Federrath et al. 2020).

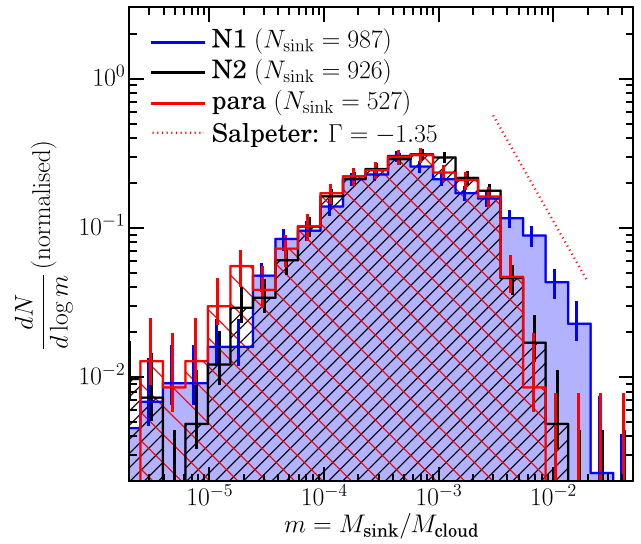


Figure A2. Logarithmic mass function $dN/d \log m$ of the sink particles from the N1 (blue shaded histogram) and N2 (black densely hatched histogram) simulations as in the main part of the article, and with the *para* (red coarsely hatched histogram) simulations added (all at SFE = 10 per cent). To facilitate the comparison, we normalize the histograms so that the total area under the histogram is 1 for all three cases. The figure is otherwise identical to Fig. 5.

This paper has been typeset from a $\text{\TeX}/\text{\LaTeX}$ file prepared by the author.